Astronomy & Astrophysics manuscript no. S284˙Puga˙astro˙ph
July 7, 2009
© ESO 2009

arXiv:0907.1253v1 [astro-ph.GA] 7 Jul 2009

Spitzer/IRAC view of Sh 2-284 [⋆]

Searching for evidence of triggered star formation in an isolated region in the outer Milky Way

E. Puga[1], S. Hony[2,1], C. Neiner[3,1], A. Lenorzer[4], A.-M. Hubert[3], L.B.F.M. Waters[5,1], F. Cusano[6], and V. Ripepi[7]

[1] Instituut voor Sterrenkunde, Katholieke Universiteit Leuven, Celestijnenlaan 200D, 3001 Leuven, Belgium
e-mail: `elena@ster.kuleuven.be`
[2] Laboratoire AIM, CEA/DSM - CNRS - Université Paris Diderot, DAPNIA/SAp, 91191 Gif-sur-Yvette, France
[3] GEPI, Observatoire de Paris, CNRS, Université Paris Diderot; 5 place Jules Janssen, 92190 Meudon, France
[4] Instituto Astrofísico de Canarias,C/ Vía Láctea s/n, E-38200, La Laguna, Spain
[5] Sterrenkunde Instituut, Universiteit van Amsterdam, Kruislaan 403, 1098SJ Amsterdam, The Netherlands
[6] Thüringer Landessternwarte Tautenburg, Sternwarte 5, D-07778 Tautenburg, Germany
[7] INAF- Osservatorio Astronomico di Capodimonte, Via Moiariello 16, I-80131 Napoli, Italy

Received ; accepted

Abstract

Aims. Using Spitzer/IRAC observations of a region to be observed by the CoRoT satellite, we have unraveled a new complex star-forming region at low metallicity in the outer Galaxy. We perform a study of S284 in order to outline the chain of events in this star-forming region.
Methods. We used four-band Spitzer/IRAC photometry as well as Hα imaging obtained with INT/WFC. Combining these data with the optical photometry obtained in the frame of CoRoTs preparation and the 2MASS catalog we analysed the properties and distribution of young stellar objects (YSOs) associated with point-like sources. We also studied the SEDs of regions of extended emission, complementing our dataset with IRAS and MSX data.
Results. We find that S284 is unique in several ways: it is very isolated at the end of a spiral arm and both the diffuse dust and ionized emission are remarkably symmetric. We have partially resolved the central clusters of the three bubbles present in this region. Despite the different scales present in its multiple-bubble morphology, our study points to a very narrow spread of ages among the powering high-mass clusters. In contrast, the particular sawtooth structure of the extended emission at the rim of each ionized bubble harbours either small lower-mass clusters with a younger stellar population or individual young reddened protostars. In particular, triggered star formation is considered to be at work in these regions.
Conclusions.]

Key words. Stars: formation, pre-main sequence, ISM: bubbles, HII regions, ISM: individual: Sh 2-284, Galaxy: open clusters and associations: individual: Dolidze 25

1. Introduction

Several scenarios have been put forward to explain the role of expanding H II regions in the frame of triggered star formation (Elmegreen 1998; Deharveng et al. 2005). Observationally, it is difficult to find an isolated H II region in the Galactic plane where the impact of the expansion can be decoupled from severe crowding effects (see summary by Churchwell et al. 2006). However, triggered SF is commonly invoked when H II regions and bubbles are aligned and a multiple-bubble morphology is detected. Several examples of H II regions have been recently investigated a few degrees off the Galactic disk plane as an illustration of the specific hypothesis called: ”collect and collapse mechanism” (Deharveng et al. 2005; Zavagno et al. 2006, 2007). The outer region of our Galaxy offers a benchmark to study this type of object (Ehlerová & Palouš 2005). Away from the central spiral arms, the third quadrant is sparsely populated with the giant molecular clouds belonging to the Perseus and Norma-Cygnus arms. Moreover, lower metallicities are measured toward the outer Galaxy (Martín-Hernández et al. 2002), guarantee of closer conditions to the pristine initial molecular clouds.

Sh 2-284 (hereafter S284) is a diffuse nebula observed for the Sharpless (1959) catalog. This region is located in the anticentre of the Galactic disk (l=212°, b=−1.3°), and it is relatively isolated. It shows a very symmetric morphology in the red plate of the Palomar Observatory Sky Survey (POSS) with an approximated diameter of 80′ in the sky. The kinematical study of the Hα line in S284 revealed a two-component velocity profile (Fich et al. 1990). The radial velocities of these components are 43.0±0.5 and −20.1±0.5 km s^{-1}, while the linewidths are 48.6±0.5 and 26.4±0.8 km s^{-1}, respectively. Later studies of several recombination lines at 9 cm toward S284 (Lockman et al. 1996) encountered similar values for this first velocity component (V=45.2±1.5 km s^{-1}, ΔV=28.2±3.6 km s^{-1}). The narrow linewidths of the ionized gas tracers toward S284 are compatible with a diffuse H II region origin. These estimates of the radial velocities agree with the values obtained from the observation of the CO emission (see Blitz et al. 1982; Wouterloot & Brand

---

Send offprint requests to: E. Puga

[⋆] Based on data obtained with IRAC onboard Spitzer (Program ID 3340) and the WFC at Isaac Newton Telescope at La Palma.

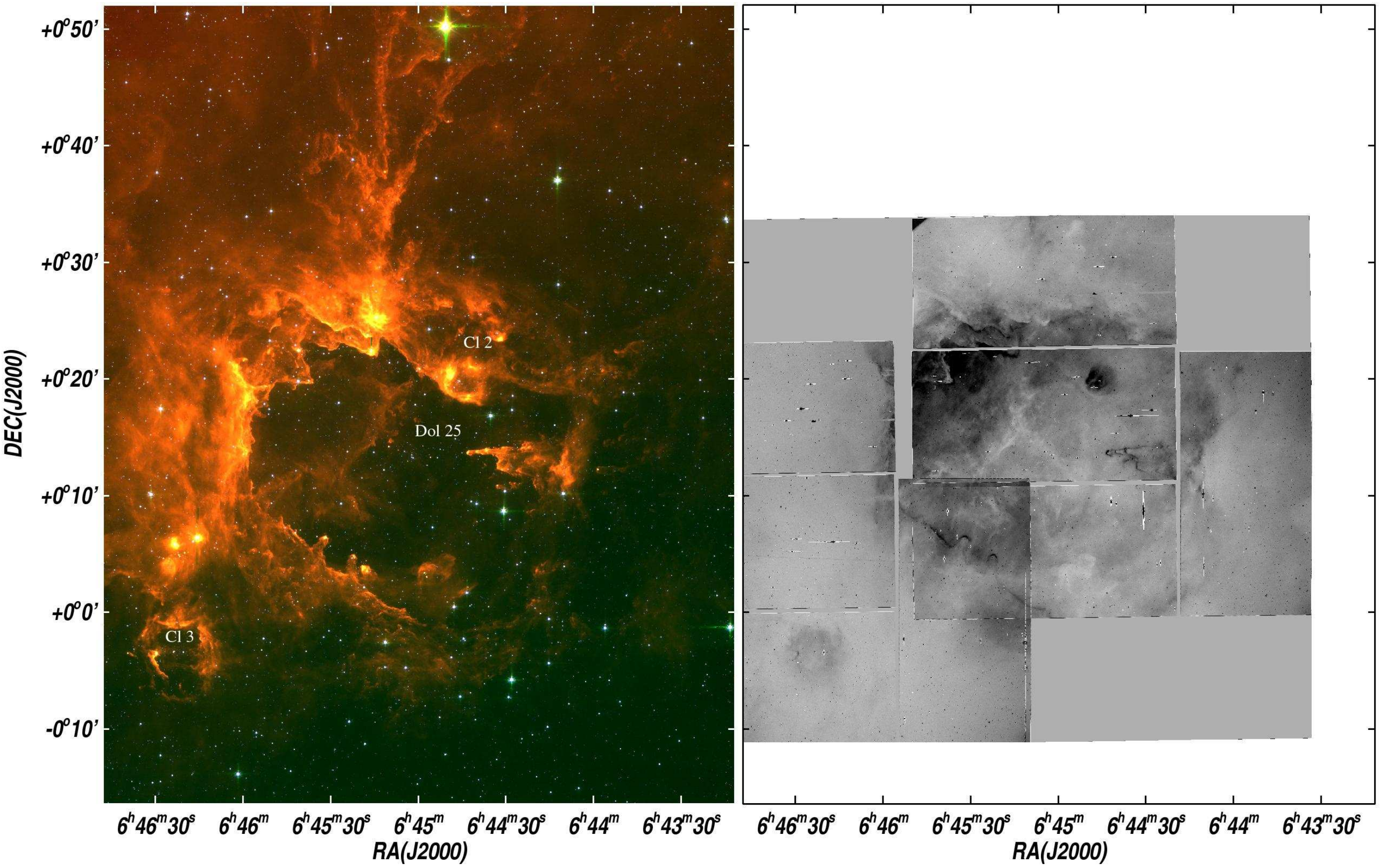

Figure 1. (Left panel) Colour-composite image of S284 with IRAC (*blue*: IRAC 3.6, *green*: IRAC 5.8, *red*: IRAC 8.0). **(Right panel)** Inverted grey scale of the Hα emission of S284 obtained with the WFC at the Isaac Newton Telescope. The image is in arbitrary units.

1989). Radial velocities in the range V_{LSR} ~42.0–46.8 km s^{-1} have meen measured at various locations in the field, yielding heliocentric distances between 5.2 and 6.5 kpc.

S284 hosts a cluster of stars in its centre known as Cl Dolidze 25 (Dolidze 1961); aka C 0642+0.03 or OCL-537. The stellar population of this cluster was initially characterised through UBV–Hα photometry by Moffat & Vogt (1975). They concluded that Dolidze 25 was a cluster of 10 O and B type stars and 1 F supergiant. However, in their study of a $23' \times 16'$ field, the authors separated the cluster into two subclusters with different reddening. A northern group of foreground stars of E($B-V$)≈15 at a distance of 0.75 kpc and a redder and more concentrated central cluster. Turbide & Moffat (1993) have pinned down its reddening to E($B-V$)≈0.83 and the distance to 5.0 kpc, allowing for a metallicity gradient in the Galactic rotation curve. These results cast doubt on the physical connection between the different clusters found in this field. Although much has been discussed about the actual members of the cluster (see Babu 1983; Turbide & Moffat 1993; Pandey et al. 2006), most authors agree on the distance to the central concentration of stars. Russeil et al. (2007) recalculated this parameter using previous UBV photometry and spectroscopy (Moffat et al. 1979a; Turbide & Moffat 1993) yielding a distance of 6.03±1.16 kpc. However, the selected stars to derive this value do not belong to the central subcluster. A more recent spectroscopic study of the sources Dol 25–15, Dol 25–17, and Dol 25–22 within this central subcluster (Lennon et al. 1990) the authors determined: (i) earlier spectral types than prevously derived for these sources, (ii) the low metallicity of the cluster ($Z=0.17\,Z_{\odot}$), (iii) a spectrophotometric distance of 5.5±0.5 kpc. We adopt a distance of 5 kpc throughout the present study. The age of the cluster (7 Myr) has been estimated through isochrone fitting of precision photometry in the $4' \times 4'$ field around Dolidze 25 (Turbide & Moffat 1993).

Water-maser emission has been detected toward a few locations around S284 (Wouterloot et al. 1988; Brand et al. 1994), whereas no SiO, CS, or methanol maser emission (i.e. tracers of very dense ambient material) have been detected (Harju et al. 1998; Plume et al. 1992; Zinchenko et al. 1998; Bachiller et al. 1990).

The objective of this paper is to determine the properties of the different regions identified toward this site and their physical interconnection. In particular, it focuses on scrutinizing the evidence for sequential star formation.

This article is structured as follows. In Sect. 2 we describe the observations of this star-forming region (SFR), obtained with Spitzer/IRAC (Sect. 2.1). We also present ground-based Hα observations obtained with INT/WFC (Sect. 2.3), as well as additional optical data, which we cross-correlate with 2MASS and Spitzer/IRAC. Secondly, we focus on the stars and distribution of young stellar objects (Sect. 3.1), followed by an analogous study of blobs of extended emission (Sect. 3.2). In Sect. 4 we discuss the spectral types of the stellar content in S284 (Sect. 4.2) and the relative ages and timescales we determine (Sect. 4.3). In Sect. 4.1 we discuss the uniqueness of this nebula in terms of its particular environmental conditions. Finally, conclusions are drawn in Sect. 5.

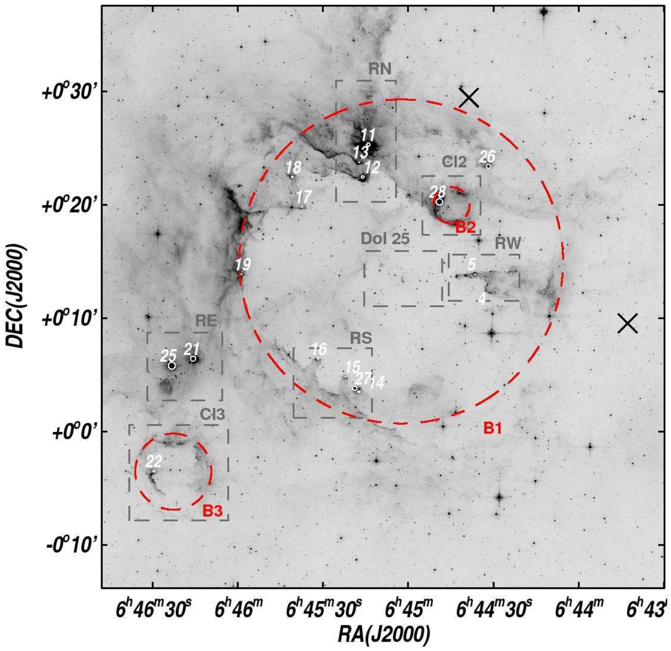

Figure 2. Map of S284 in the IRAC 5.8 band in logarithmic scale. The bubbles are identified with large discontinuous circles to guide the eye, blobs are represented by small circles, and discontinuous boxes indicate the selected regions for close-up study. The x-symbols correspond to the H_2O maser emission reported by Brand et al. (1994) and Wouterloot et al. (1988).

2. Observations and data reduction

2.1. Spitzer/IRAC Imaging

We observed S284 with the IRAC (InfraRed Array Camera) onboard Spitzer during Cycle 4 (2005 March 28) under Programme ID 3340. The observations were conducted in the four IRAC filters at 3.6, 4.5, 5.8, and 8.0 μm (Fazio et al. 2004). S284 spreads over an area of $1^\circ \times 1\fdg4$ with its centre at $\alpha_{2000} = 06^h\,45^m\,00\fs0$, $\delta_{2000} = +00^\circ\,17'\,56\farcs9$. We performed a raster map with IRAC mapping mode in each filter with a spacing between rows of $1/3^{\rm rd}$ of the camera field of view ($5\farcm2 \times 5\farcm2$). The IRAC simultaneous imaging in two consecutive filters results in an offset for two of the mosaic fields of around $6\farcm8$ (in our case, in declination). A final area, covered in all filters, of approximately $0\fdg95 \times 1\fdg3$ was obtained. We obtained an average integration time of 80.4 seconds per sky pixel.

The Spitzer Science Center provided the Spitzer/IRAC basic calibrated data (BCD), using the pipeline version S11.4.0. Further treatment of the images with the contributed IRAC software was necessary to correct for the muxbleed and pulldown effects of the detector. Likewise, the difference in the background levels of overlapping frames present in the IRAC 8.0 μm channel was corrected with the post-BCD overlap correction software. Subsequently, we used the dedicated software package MOPEX (version 030106) to produce mosaics of the IRAC images and to perform PSF photometry (Makovoz & Marleau 2005).

MOPEX performs image interpolation and co-addition of the individual images onto a common grid. Moreover, it allows outlier rejection through four different algorithms. Considering the shallow coverage of the field, cosmic rays and other outliers were removed using the box outlier and dual outlier MOPEX modules. The mosaic final pixel scale corresponds to the original $1\farcs22$/pix. An image of this field in three IRAC colours is shown in Fig. 1.

The source extraction is preceded by the construction of our own point response function (PRF i.e., an oversampled PSF). We selected 30 isolated bright stars by hand from the final mosaic for each filter. The postage stamp images of these sources were resampled to 1/4th. We normalized the PRF for a radius that encompasses the first Airy ring for each band, therefore an aperture correction needed to be applied for the extracted flux on each single channel. The presence of strong filamentary extended emission in the four bands required the use of a small-width median filter for a proper background subtraction (11″ for IRAC 3.6 μm and IRAC 4.5 μm and $6\farcs35$ for IRAC 5.8 μm and IRAC 8.0 μm). This aggressive filtering was accordingly applied to the channel PRF, producing an underestimate of the source flux. The correction factor was determined from the flux ratio between the unfiltered and filtered PRFs (Shenoy et al. 2007).

The source detection was performed in the single final coadded frame for each individual channel. To ensure a high reliability, we only selected sources with $S/N > 5$. We finally obtained extraction lists of 124 657, 118 289, 19 445 and 15 856 sources in the IRAC 3.6, 4.5, 5.8, and 8.0 μm channels, respectively (hereafter referred to as IRAC 3.6, IRAC 4.5, IRAC 5.8, and IRAC 8.0). The final merged list of the four bands was obtained by matching the coordinates of the extracted sources in the four bands (using an optimally determined maximum distance of $1\farcs5$). To minimize the contamination by spurious detections in the source catalog we apply a filtering criterion based on simultaneous detection in multiple filters. We require detection of the object in either the two bluest (IRAC 3.6 and 4.5) or reddest bands (IRAC 5.8 and 8.0). This criterion accomodates faint blue sources and very red sources allowing them to survive into the source list. A total of 8 010 sources were extracted in the four filters. Since the IRAC/Spitzer observations were aimed at relatively faint sources, very bright objects appear saturated in our images. We determine the saturation limit of each band by comparison of the fluxes obtained with PRF fitting and aperture photometry (aperture radius of 3 pixels). The limit is set by eye at the beginning of the nonlinear regime between these two fluxes.

2.2. Cross-correlation with 2MASS

In addition to the Spitzer/IRAC we used the 2MASS catalog. We cross-correlated the point sources found in the IRAC images with this catalog to obtain J-, H-, and K_s-band photometry. At least one of these colours was found in 2MASS for 23 734 point sources at a distance closer than $1\farcs5$.

2.3. Cross-correlation with INT/WFC

Since the field containing S284 is a target field of the CoRoT satellite, it has been studied by CoRoT's exoplanet team led by M. Deleuil (Deleuil et al. 2009). As a preparation for the CoRoT mission, this team obtained 6187 images in CoRoT's fields with the WFC (Wide Field Camera) at the 2.5m INT (Isaac Newton telescope) in La Palma (Spain), in order to classify the stars and select the best candidates for planetary transits. They used the B and V Bessel filters and the r' and i' Sloan Gunn filters. See Deeg et al., in preparation for more details. The exoplanet team of CoRoT kindly put at our disposal the photometry they derived in these four filters from their observations for the field of S284.

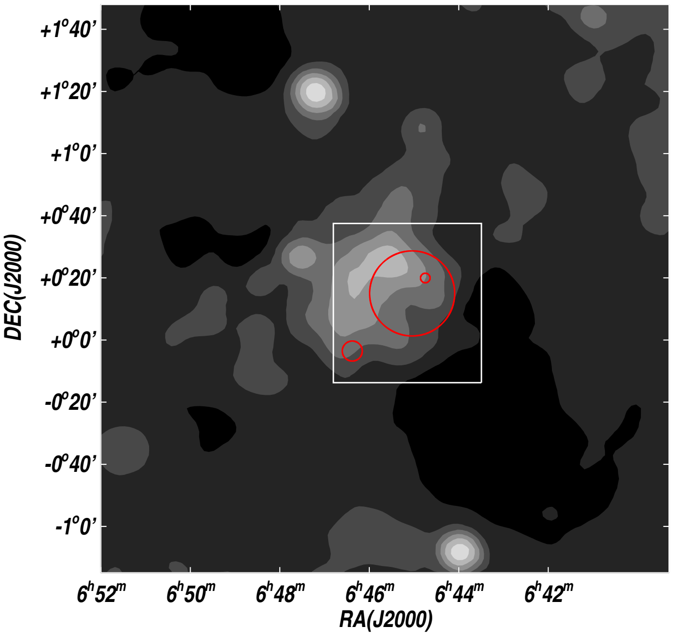

Figure 3. Map of the A_V extinction in the $3^\circ \times 3^\circ$ region around S284. The logarigthmic filled contours correspond to A_V =[1.5, 2.25, 3.3, 4.7, 6.9, 10.0, 14.5, 21.1] mag. The white box corresponds to the field of view shown in Fig. 2. The bubbles identified in S284 are represented with circles.

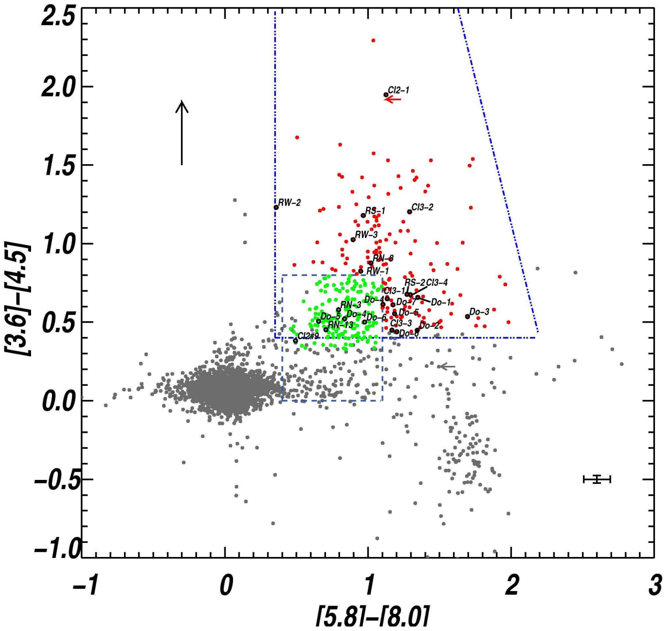

Figure 4. IRAC colour-colour diagram of S284. The dots represent the objects that are detected in the four IRAC bands, while arrows correspond to the limiting position of objects that appear saturated in the IRAC 8.0 band. Median photometric errors are indicated with the error bars in the bottom right corner. The boundaries of the regions for Class I and Class II objects are taken from Allen et al. (2004). The black arrow represents a reddening vector for a visual extinction of 30 mag.

The mean seeing of the data for this field is about 1.5″and the mean astrometric error is 0.06″.

In addition, we have obtained specific observations of S284 in 2005 December 18 with the same instrumentation (WFC/INT) with a focus on the extended emission. We used the Hα and (λ 6568) Sloan Gunn *r'* filters to trace the recombination line and continuum, respectively. Two pointing positions were needed to cover the nearly $1^\circ \times 1^\circ$ region. We obtained two exposures of 1200 s in Hα and 300 s in *r'*. After bias, flatfield, and astrometry corrections, the 4 different CCDs were independently corrected for optical distortions with a 3$^{\rm rd}$ order polynomial. The different exposures and pointings were combined with the IRAF routine MSCRED. Subsequently, the stellar continuum was subtracteed in order to obtain a line emission image. After exposure time synchronization, the *r'*-band mosaic was multiplied by the flux ratio of 23 stars in the field in both bands. Since we are interested in the extended emission, no absolute flux calibration was performed on the data. The Hα (continuum subtracted) image is shown in the right panel of Fig. 1.

3. Results

Large dust bubbles are ubiquitous in the Galactic plane toward the Galactic centre as shown by the GLIMPSE Survey (Churchwell et al. 2006). However, the study of these structures is being hampered by the difficulties imposed by crowding effects, the strong background toward the Galactic midplane, and the frequent asymmetries in the bubbles as a result of interactions with closeby regions.

The unprecedented view of S284 in the mid-IR provided by IRAC/Spitzer (see Fig. 1 *left panel*) has revealed in detail the presence of complex extended emission in this region, which was not previously detected in 2MASS observations. The emission is present in all four IRAC bands implying diffuse dust emission. This interpretation is corroborated by its detection (although at much poorer resolution) in IRAS maps, even at 100 μm. The mid-IR emission appears the strongest in the IRAC 8.0 band, since this band contains the PAH band emission at 7.7 μm and 8.6 μm. On the largest scale toward S284, the images reveal that the dust shells bound the bright Hα emission quite well (see also Fig. 1 *right panel*), therefore tracing the photon-dominated regions (PDRs) and the dense swept-up shells. These two complementary maps allow us to identify three bubble-like structures shown in Fig. 2. In fact, the IR emission extends well beyond the 18-pc inner bubble radius of the largest bubble (hereafter B1). The dust emission almost fully surrounds the ionized gas although it appears less prominent to the southwest, likely due to a density gradient within the molecular cloud. This is also evident on the much larger scale traced by the Schlegel et al. (1998) Galactic dust extinction map (see Fig. 3), where lower extinction values are detected in this direction. In the same direction, the Hα map shows a faint extended emission component. This leak of ionizing photons suggests that the H ii region may be density-bound to the southwest. The OB cluster Dolidze 25, as outlined by Turbide & Moffat (1993) and Babu (1983), is located at the geometrical centre of B1. Interestingly, our Hα image (Fig. 1 *right panel*) traces the bright rim of dense ionized gas, especially bright to the southeast of the ionized bubble.

The resolved filamentary structure of the dust allows differentiating among several other regions in the field of S284. Another two shells of dust enclose more compact H ii regions within the field around S284. The bubble B2 is located to the northwest, sitting amidst the ionized emission of B1 and yet very close to its rim. This compact bubble (diameter∼ 3.5 pc), seems associated with IRAS06422+0053 which is the brightest point-source at 100 μm. The low extinction observed toward this area of ionized gas, together with the higher brightness in Hα indicate

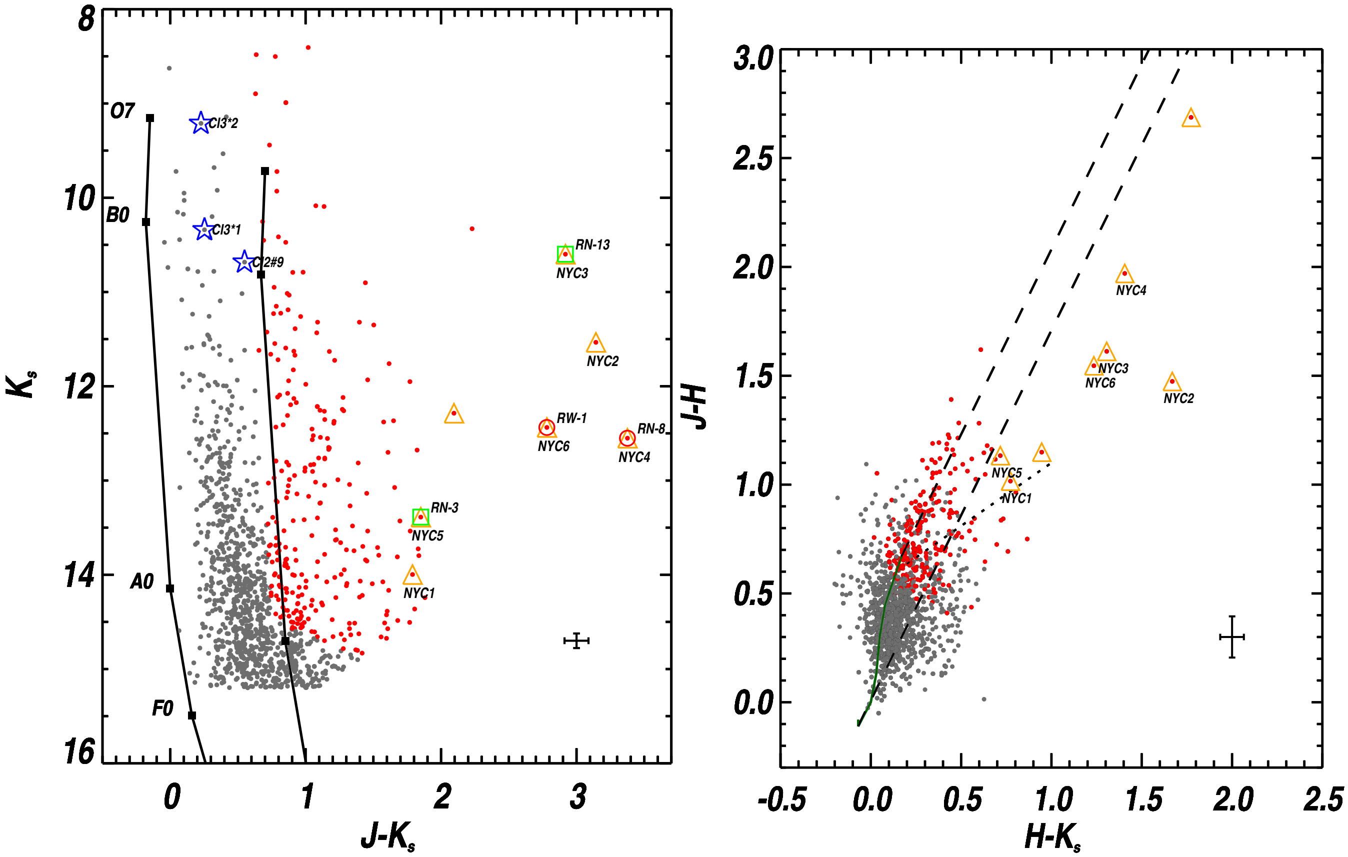

Figure 5. (Left panel) 2MASS colour-magnitude diagram of the stellar content within the square areas indicated in Fig. 1. The lines connecting the small squares represent the main sequence of luminosity class V stars without extinction and with $A_V \sim 5$ mag. The labels correspond to sources further discussed. **(Right panel)** 2MASS colour-colour diagram of the same regions. The dashed lines indicate the direction of extinction according to an α =1.61 extinction law (Rieke & Lebofsky 1985). The dotted line represents the T Tauri locus of Meyer et al. (1997). Therefore, the triangles highlight sources with near-IR excess (YSO candidates). Median photometric errors are represented by crosses in the lower-right corners of both diagrams [see the electronic edition of the Journal for a colour version of this figure].

that it is probably located in the foreground of B1. We detect a stellar cluster in its centre labelled as Cl2 (see the left panel in Fig. 1). Two of the sources of Cl2 belong to the trail of stars that has often been associated with Dolidze 25.

A third bubble of 4-pc diameter lies within the mid-IR emission and is located to the southeast of B1. The ionized gas is barely detected in the INT Hα mosaic. This source coincides with IRAS06439-0000 and IRAS06439+0111. We report the detection of another stellar cluster (labelled as Cl3) at the centre of B3. Overall, these three bubbles show a remarkable symmetry despite the highly probable interaction among them.

Another prominent type of structure observed toward S284 are several cometary globules that are detected at the rim of bubble B1. These globules appear in emission in the IRAC images and as absorption silhouettes in the Hα image. Moreover, they appear highlighted in the latter map by the presence of ionization rims at the head of the globules. All of them point toward the centre of B1 showing very diverse stellar content (see next section) and morphology with their location around the nebula. Globules to the northeast show wide tails and harbour resolved clusters of sources. They also seem to be located at various radial distances from Dolidze 25, possibly due to a projection effect (e.g. the region labelled as RN in Fig. 2). The cometary globules or elephant trunks to the south and west possess longer and thinner tails and only contain a few unresolved sources at the head, in IRAC 3.6 and 4.5.

As measured by the shielded material behind the condensations, this distinctive morphology between cometary globules and elephant trunks supports our hypothesis of a density gradient in the ambient material. However, observations of the molecular gas are needed to confirm this statement.

Bubble B3 shows only one cometary globule at the eastern rim of the dust bubble. A resolved source appears in the head of this cometary structure, which points to cluster Cl3. Some of these globules and trunks are associated with isolated IRAS sources, indicating an enshrouded nature. Discussion on their stellar content follows in the next section.

3.1. Stellar content: point-like sources

Our IRAC/Spitzer data has unveiled the presence of a rich stellar population in S284 in the form of various peripheral clusters. It also allows us to put constraints on the debated extent of the cluster members of Dolidze 25 through the link between cluster and larger dust structures. Another important point is the inferred presence of high-mass stars in clusters Cl2 and Cl3 through the detection of associated ionized regions, which requires the existence of at least one star of spectral type earlier than a B3V (Churchwell 2002).

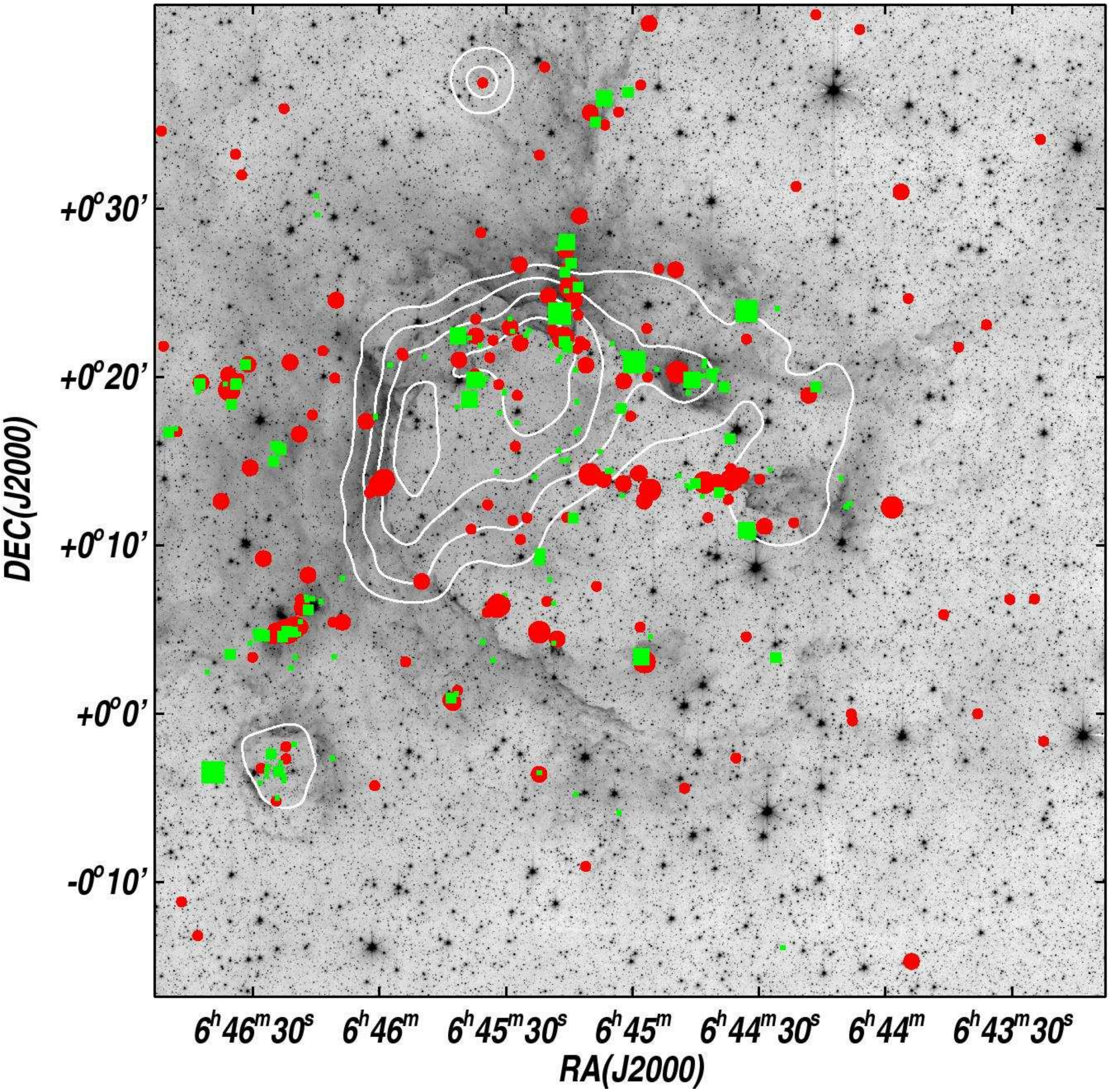

Figure 6. Distribution of young stellar objects in the field around S284 on the IRAC 3.6 map. Class I objects are represented by filled red circles and scaled in size with the IRAC 4.5 brightness in the range 8.2–17 mag. Class II objects are depicted with filled green squares and scaled in size with the IRAC 5.8 magnitude in the range 7.9–14.35 mag . Open circles correspond to possible Class I objects that appear saturated in IRAC 8 μm. White contours represent the radio continuum emission detected from the 4850MHz survey (Condon et al. 1991)[see the electronic edition of the Journal for a colour version of this figure].

Our mid-IR IRAC data allows the classification of point-like sources based on the differentiation between sources that show an IR excess and those that are photosphere-dominated. Furthermore, it is also used as a young stellar object subclassification between Class I and Class II objects by comparison with models of proto-stellar envelopes and circumstellar disks (Allen et al. 2004). The effective temperature and luminosities of young stars can be used to infer their ages and thus the timescale for the different evolutionary stages of the circumstellar material. Although the literature comprises information on the spectral types of a small sub-sample of bright stars (Lennon et al. 1990; Moffat & Vogt 1975; Babu 1983), the reported spectral types vary significantly; for instance, the spectral type clasification of the brightest source in Cl2 –an A0 star according to Babu (1983)– is not sufficient to produce the observed H II region. As an alternative, a crude estimate of the spectral type can be derived from the stellar brightness in the IRAC 4.5.

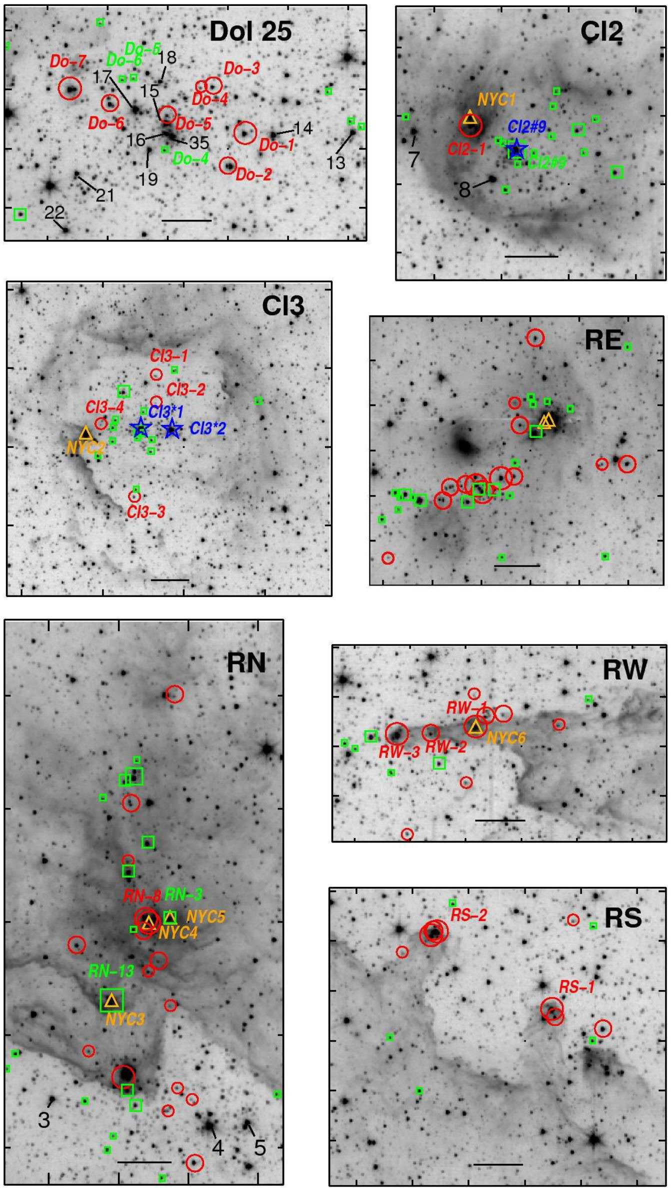

Figure 7. Individual regions in S284 overlayed on the IRAC 3.6 map. Symbols correspond to Class I objects (*red circles*), Class II objects (*green squares*) and near-IR excess sources (*orange triangles*). Blue stars mark the location of the powering stars in Cl2 and Cl3. Horizontal bars represent a scale of 1′. Black labels correspond to the source ID given in Moffat & Vogt (1975) [see the electronic edition of the Journal for a colour version of this figure].

3.1.1. IRAC/Spitzer colour-colour diagram

Our IRAC observations open a new window on the stellar content in S284. This improvement does not come so much from peering through the extinction at longer wavelengths, but from the fact that the sensitivities achieved in IRAC 3.6 and IRAC 4.5 are higher than existing near-IR surveys. Our mid-IR colour-colour stellar classification is restricted by the limiting magnitudes in IRAC 5.8 and IRAC 8.0 (14 and 13.5 mag, respectively), since simultaneous detection in the four bands is needed for this classification method. In addition, to increase the reliability of our classification, we only consider those objects with photometric error smaller than 0.175 mag in each of the four bands.

The diagram using a total of 4046 sources is presented in Fig. 4. Bona fide candidate Class I objects are selected from the region marked in the diagram with the restriction that [3.6]−[4.5]>0.4 mag. The bulk of main sequence and giant stars is centred at a [3.6]−[4.5]=+0.1 mag, thus on average slightly bluer than expected. As a consequence, main sequence and giant stars contaminate the area of the diagram where Class II objects lie according to the models (Allen et al. 2004). For this reason, we have designated as Class II sources those whose [3.6]−[4.5] colour is above the visible gap in this direction, namely [3.6]−[4.5]> 0.3 mag. A particular group of sources lies in a region of the diagram where [5.8]−[8.0]> 1.4 mag and [3.6]−[4.5]< 0 mag. These points correspond to enhancements in the filamentary extended structure that MOPEX detected as point-like sources whose colours correspond to reflected emission, i.e., reflection nebulae.

The full lists of Class I and Class II candidates are available electronically in Tables 3 and 4.

3.1.2. 2MASS diagrams

The complementary information provided by the 2MASS catalog is especially useful for the brightest stars that appear saturated in our IRAC images. This is the case for bright central sources located in the heads of a few cometary globules. It is important, however, to bear in mind the slightly lower spatial resolution of the 2MASS survey, especially toward the centre of the more dense clusters. The near-IR colour-magnitude and colour-colour diagrams of the sources within S284 are displayed in Fig. 5.

For the colour-magnitude diagram (CMD), we consider sources with relative photometric error below 20% in the three 2MASS bands. The main sequence (MS) at a distance of 5 kpc with $A_V = 0$ and $A_V = 5$ mag are displayed for reference. Note that the estimated average extinction toward Dolidze 25 corresponds to $A_V = 1.98$ mag (Turbide & Moffat 1993). The M_V magnitudes of luminosity class V are obtained from Schmidt-Kaler (1982). For the colours of the spectral types earlier than A0V we use the values from Wegner (1994) and for later spectral types we obtained the colours from Tokunaga (2000). The near-IR extinction law adopted is from Rieke & Lebofsky (1985). We select the sources redder than the gap noticeable at $J - K_s \sim -0.3$ mag in our CMD and brighter than an accordingly reddened star B8V (points represented in red in Fig. 5). These objects are either intermediate- and high-mass stars that are strongly reddened or more evolved stars that have reached the giant phase. These presumably reddened stars are plotted in the colour-colour diagram (CCD) shown in Fig. 5 (*right panel*), where many of them lie in the red giant locus.

In our CCD we consider that stars posses a near-IR excess when they appear redward of the region limited by the reddening vectors projected from the intrinsic colours of main sequence stars and giants and above the T Tauri locus (Meyer et al. 1997). These objects (marked with triangles in the diagram) are considered to be YSO candidates (Ojha et al. 2004). The same triangle-like symbols are used to highlight those objects back on the CMD.

3.1.3. The distribution of YSOs

The spatial distribution of YSO candidates in S284 is shown in Fig. 6. The symbol sizes for the Class II candidates are scaled with the IRAC 4.5 brightness as a proxy for the luminosity of the YSO (Whitney et al. 2004). This choice is motivated by the fact that the PRF is undersampled in the IRAC 3.6 band, while oversampled in the other bands; IRAC 4.5 thus offers a more reliable measure of the flux. Moreover, the extended emission appears least prominent in the 4.5 μm map. Analogously, the symbol sizes for Class I objects are proportional to the IRAC 5.8 brightness. Although IRAC 8.0 seems better suited to YSOs with a strong excess, the 7.7 μm PAH emission band could contribute significantly to the source flux estimate (Peeters et al. 2002).

Most Class I and Class II candidates arise in clusters around the shell of the B1 dust bubble or at the locations of the powering clusters Dolidze 25, Cl2, and Cl3. Other YSOs around B1 seem to be more scattered, but for some cases their low brigthness make them dubious. Several bright Class I objects are located at the head of cometary globules or at elephant trunks around B1. In particular, the longest trunk of the region harbours several Class I candidates at various positions along the trunk (RW in Fig. 2). Those candidates at the rim of the B1 bubble show a colour [3.6]−[4.5]> 1.1 mag indicative of either strong reddening or high stellar temperatures Whitney et al. (2004). We also detect two clusters of Class I and Class II objects (RE in Fig. 2 and another concentration 15′ north of RE) a few parsec distant from the ionization front associated with B1. To the north of the IRAC field, we find one isolated Class I candidate at the centre of a region of strong radio continuum emission.

Surprisingly, Dolidze 25 comprises several Class I objects located in a 4′ projected diameter region. This result will be discussed further in Sect. 4.3. Cl2 and Cl3 seem to have a small population of YSOs dominated by Class II objects, whereas a Class I candidate is detected at the rim of each bubble. In conclusion, the location of the YSO candidates follows closely the morphology of the nebulae. There is a higher concentration of young objects along the IR bright rim of B1. However, a significant number of objects are detected as far as few tens of parsecs away from the rim of B1.

3.1.4. Comments on the stellar population of individual regions

Dolidze 25 Most of the objects that have been traditionally considered as members of Dolidze 25 (e.g. #17, #15, #16, #35, #22, #18, #19) do not show any circumstellar peculiarity at near- and mid-IR wavelengths (see Fig. 7). A concentration of Class I candidates exists toward Dolidze 25, while low-luminosity Class II sources appear more scattered around the cluster. Most of the Class I candidates are also detected in the *J* band ruling out the possibility of being reddened Class II objects.

Cl2 The area around Cl2, also including B2, shows a high concentration of Class II objects. The source located at the centre of the cluster (source #9 in Table 2) has been spectroscopically classified in the optical as an O9V star (Moffat et al. 1979b). The cluster core appears elongated at mid-IR wavelengths and starts to be resolved redward of 5.8 μm. The counterpart to O9V star exhibits the mid-IR colours of a Class II object, although this could be due to the contamination by the nearby object. Another source observed in the direction of the H II region (#8) appears extended in our IRAC 3.6 image and is barely resolved into two point-like sources in the redder IRAC maps. A bright Class I object is detected at the rim of the dust bubble, where the extended emission is the strongest. Another nearby object shows a strong near-IR excess (NYC1).

Cl3 The two brightest objects within the central cluster (Cl3*1 and Cl3*2) are detected in all four IRAC bands, but their SEDs only show a photospheric component. Their location in the near-IR CMD suggests that these are O-type stars. In particular, Cl3*1 is closely surrounded by sources that show a mid-IR excess. NYC-2 is located at the head of the cometary globule east of bubble B3 and appears saturated in IRAC 3.6, IRAC 4.5, and IRAC 8.0, so it is not included in our analysis of Sect. 3.1.1. However, the overall shape of its SED corresponds to a Class I candidate.

RN The field labelled as RN includes several cometary globules to the north of B1. Two of the brightest sources at the vortices of cometary globules appear saturated in one of our IRAC maps, and yet, bright Class I objects are unveiled within these clusters, pointing to the presence of various YSOs embedded in these regions. The detection of two Class II candidates (RN-13 and RN-3) is reinforced by the near-IR excess shown in the 2MASS photometry (sources NYC3 and NYC5). One of them coincides with the head of a non-saturated globule that hosts only few point-like objects.

RE The field RE has two blobs of strong emission separated by a projected distance of ~0.4 pc. The eastern blob is resolved into extended emission, while the western blob has several resolved point-like sources, the central one saturated. The 2MASS photometry toward this source reveals a near-IR excess at a slightly worse resolution than our IRAC images. A resolved cluster is detected to the south of the blobs. Seven bright Class I candidates are aligned in a trail, while several Class II sources are scattered around. This cluster is partially detected in the near-IR and optical, indicating that it is not deeply embedded within the dust; hence, we can rule out that the Class I candidates are reddened Class II objects. Moreover, these Class I candidates are the only objects not located at the rim of B1 that show a colour [3.6]−[4.5]> 1.1 mag, pointing to relatively high luminosities (Whitney et al. 2004), but not hot enough to generate an H II region.

RW and RS The region RW encompasses the longest trunk at the rim of B1. Several Class I objects are located along the pillar. One of them is also detected by an associated near-IR excess.

Analogously, the RS region contains another two trunks that harbour Class I sources at the head of their cometary globules.

3.2. *Stellar content: embedded objects and blobs*

The previous sections have focused on the stellar classification of point-like sources in S284. However, the filamentary high-density structures detected in our IRAC maps support the possible presence of embedded clusters in regions where the emission appears resolved.

We selected 11 blobs or regions of small extent (a sub-scale of bubbles B2 and B3) and high infrared brightness in order to search for young embedded clusters. The radius of these blobs was defined as 1.25 × HWHM in the IRAC 8.0 band and kept constant to calculate the integrated flux in other bands. The same radius was used to search for near-infrared counterparts in the 2MASS point-source database. When multiple sources were present, we summed their contribution to estimate the total near-infrared flux. For the objects that saturated an IRAC-band image, we considered the IRAC fluxes as a lower limit and MSX fluxes

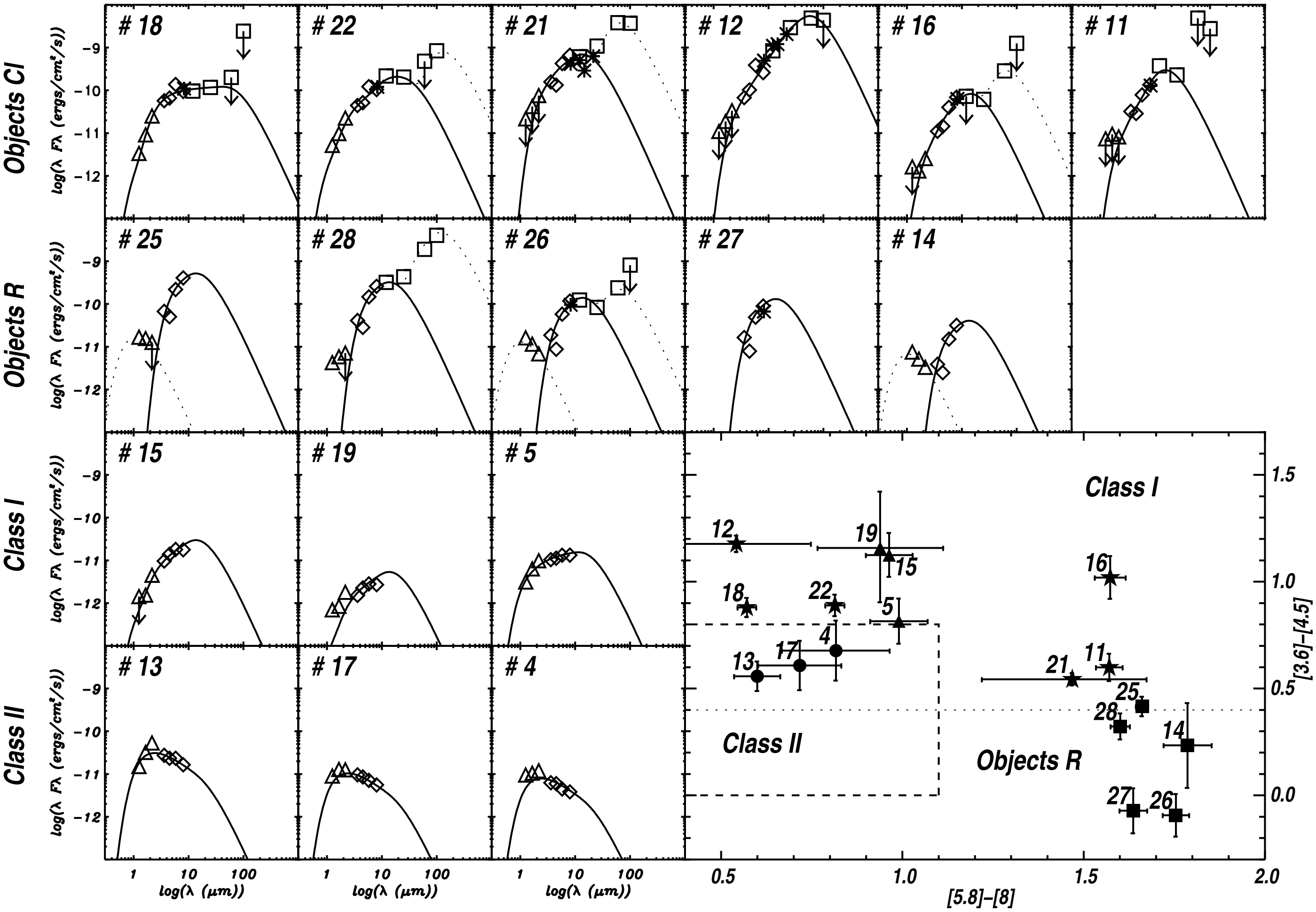

Figure 8. SEDs of the 11 blobs identified in the field of S284. The solid lines represent the total black-body distribution taken into account to compute the luminosity. The dotted lines show additional components required to better match the overall distribution. (Bottom-right panel) IRAC colour-colour diagram of the blobs. Symbols correspond to Class I unresolved objects (*triangles*), Class II unresolved objects (*circles*), blobs with reflection colours (*squares*), and blobs with colours of an early cluster phase (*stars*).

when available. We also searched for far-infrared counterparts in the IRAS point sources catalog and selected these that are compatible with the blobs as their main contibutors in the IRAS beam on the basis of HIRES images. As expected, the more extended blobs are more likely to have an IRAS counterpart.

All these data points were used to build the spectral energy distributions of the blobs presented in Fig. 8. We fitted the 2MASS, IRAC, MSX and IRAS flux distribution with a combination of blackbodies with temperature ranging from 30 to 1000 K to reproduce the shape of the SEDs and estimate their corresponding luminosities. Figure 8 displays the spectral energy distribution as well as the results of the fit. The blob characteristics are described in Table 1, while their location and radius are represented in Fig. 2.

We identify four different types of SEDs in column (6) of Table 1: (I) ClassI objects unresolved in IRAC 8.0 and with integrated near-infrared luminosities < 2.0; (II) ClassII objects, also all unresolved in IRAC 8.0; (R) objects having reflection colours; and (Cl) objects falling in the Class I region in the IRAC colour-colour diagram with higher near-infrared luminosities. This last category also tends to have a steeper 3.6 to 8 μm slope than unresolved ClassI objects, nearly as steep as reflection objects for some of them. Still, their mid-infrared spectrum cannot be fitted with a single temperature blackbody, but on the contrary require an extended range of temperatures. Their luminosity, extent, and spectral distribution suggest that these are young clusters, either constituting an earlier cluster phase compared to bubbles B2 and B3 or lower-mass clusters.

4. Discussion

4.1. Environmental conditions

Before we consider the stellar content and the ages of the various distinct regions, it is instructive to debate the global morphology and what can be concluded from it. The shell thickness of dynamically blown bubbles is a function of the central star, the age of the bubble, and the density of the ambient ISM (Weaver et al. 1977). The theory predicts that the ratio of shell thickness to radius increases with age and ambient interstellar density. Therefore, for relatively symmetric bubbles with the powering star(s) located at the geometrical centre (as is the case of S284), a smaller ratio is indicative of a lower ambient density. We observe that the ratio of shell thickness to radius is not constant around B1, decreasing along the southwest direction. A lower ambient density in this direction would explain this effect and support our interpretation of the lower dust extinction values inferred from the IRAS maps as caused by a local ambient density gradient in this direction.

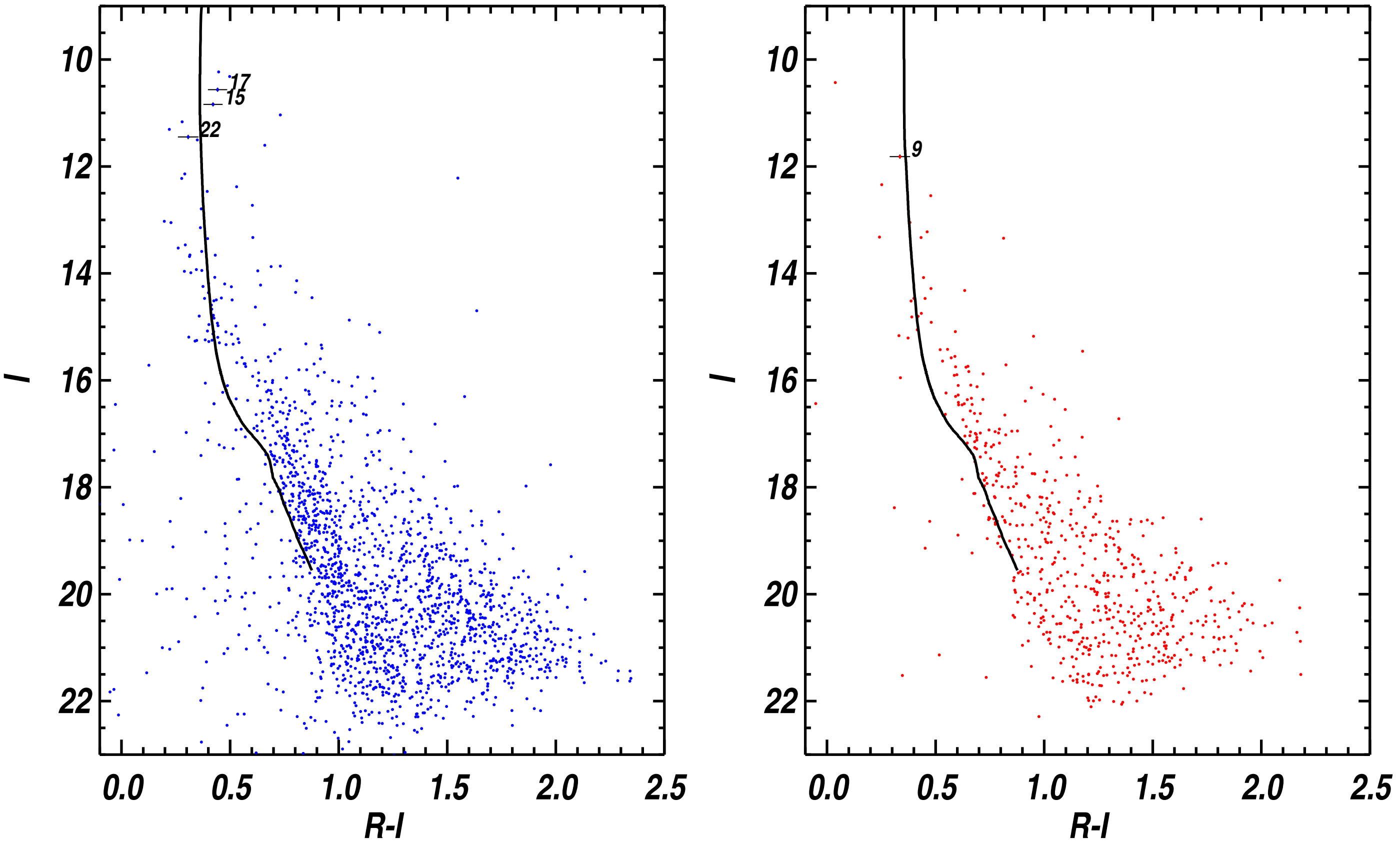

Figure 9. (Left panel) Colour-magnitude diagram of the field around Dolidze 25 combining VIMOS and INT/WFC photometry (Cusano et al. 2008; Deleuil et al. 2009). The overplotted isochrone corresponds to a log(age[yr])=6.75 and Z=0.004 (Lejeune & Schaerer 2001). The distance modulus corresponds to 14.4, while E($R-I$)=0.5 mag. **(Right panel)** Analogous colour-magnitude diagram for Cl2 with an overlayed isochrone of log(age[yr])=6.0. [See the electronic edition of the Journal for a colour version of this figure].

The presence of elephant trunks suggests that the dynamics of the H II region within B1 are dominated by the thermal pressure of the gas at 10^4 K and not by shocked gas, either produced by stellar winds or supernovae. These sawtooth shapes have been successfully modelled as the result of dynamic instabilities in the ionization front of an expanding H II region, regardless of pre-existing density inhomogeneities, by Garcia-Segura & Franco (1996). These models account for different cooling and background conditions and outline the effect of low-metallicities (final shell temperatures are higher) into thicker shells and wider and sparser trunks.

Some characteristics of this SFR may be determined by the combined effect of the lower than solar metallicity and a gas pressure that is lower than typically found in the inner MilkyWay. High-mass stars exhibit weaker winds at lower metallicity due to the less efficient momentum transfer of the stellar radiation on the outer envelope. In a study of young SFRs in the SMC, Sabbi et al. (2008) find that the morphology of the region is not shaped by wind interaction but more by the expansion of the ionized bubble, much like what is found for S284. A second effect concerns the dust shielding. Low-metallicity environments like the LMC and SMC show a deficit of the smallest dust grains (e.g. Stanimirovic et al. 2000), which may cause the UV radiation of the newly formed stars to permeate the surrounding molecular cloud and modify the conditions over great distances (e.g. dust composition, charge state of the smallest grains, photodissociation of molecular gas, Hony et al. in preparation). It is interesting to compare this with the results of Boissier et al. (2007). These authors study the star formation in a sample of late-type galaxies using IR and UV and find that the star formation in the outskirts of these galaxies is typified by less attenuation due to the lower metallicity and that these regions are underluminous in Hα. One possible explanation for the lack of prominent Hα emission is that the lower ambient pressure makes the average star-forming cluster less massive, and as a result less very massive stars are formed. S284 might be an example of such a less massive star-formation cluster, with an O7V the most massive star detected.

4.2. Spectral types and masses

The lack of detailed information on the spectral types of the complete stellar content precludes a thorough age analysis of S284. The use of spectral types has proven useful for determining age gradients in massive clusters like the Eagle nebula (Martayan et al. 2008) and probing the disk evolution toward several Galactic SF regions (e.g. Sicilia-Aguilar et al. 2006). However, we qualitatively discuss this issue with the information presently at hand.

Table 2 compiles the spectral type and luminosity class classification and membership for S284 from the literature. The various maps tracing the dust and ionized gas complement this existing information on S284 distinguishing among the different physical structures (clusters, H II regions and bubbles).

Table 1. Characteristics of the selected embedded regions and comparison with Class I and II unresolved objects.

Blob ID	RA	DEC	Radius (”)	Log(L/Lo)	Class	Region	IRAS assoc.
18.............	06 45 40.8	+00 22 27.1	5.73	2.5	Cl		06430+0025
22.............	06 46 29.6	-00 03 29.2	6.06	2.6	Cl	Cl3	06439-0000
21.............	06 46 15.8	+00 06 26.2	15.92	3.0	Cl	RE	06437+0009
12.............	06 45 16.0	+00 22 26.9	8.24	3.9	Cl	RN	06426+0025
16.............	06 45 31.8	+00 06 26.1	5.31	2.0	Cl	RS	06430+0009
11.............	06 45 14.1	+00 25 18.6	10.86	2.6	Cl	RN	06426+0028
25.............	06 46 23.3	+00 05 48.6	22.39	2.9	R	RE	
28.............	06 44 49.1	+00 20 15.3	20.14	2.7	R	Cl2	06422+0023
26.............	06 44 31.8	+00 23 23.6	13.22	2.3	R		06419+0026
27.............	06 45 18.9	+00 03 49.2	12.80	2.3	R	RS	
14.............	06 45 17.5	+00 03 30.3	5.04	1.8	R	RS	
15.............	06 45 22.0	+00 04 49.4	U	1.7	I	RS	
19.............	06 45 58.8	+00 13 52.9	U	0.9	I		
5...............	06 44 36.5	+00 13 51.2	U	1.5	I	RW	
13.............	06 45 17.3	+00 23 45.6	U	1.8	II	RN	
17.............	06 45 37.4	+00 19 49.8	U	1.3	II		06431+0023
4...............	06 44 32.9	+00 10 52.4	U	1.2	II	RW	

4.3. Relative ages and timescales

The different spatial scales of H II regions and their distribution around S284 is suggestive of different epochs of star formation. Nevertheless, a sequence of events and causality between them must be demonstrated to confirm a triggered star-formation scenario.

Low-mass Class I objects have an estimated age of a few 10^5 yr, while Class II objects range between 10^6 and 10^7 yr (White et al. 2007). We can therefore use these two classes of protostars present in the S284 field as a relative age scale to study the interaction of young clusters (<5 Myr) with their environment.

The three dust bubbles that bound the H II regions detected on our Hα map (B1, B2, and B3) share a common morphology of cometary globules or elephant trunks. In the case of B1 and B3, they are clearly protruding into the ionized gas. The brighter young YSOs (Class I) and proto-clusters appear located at the vortices of these structures, pointing to a later formation than that of the central clusters in the H II regions. That no compact radio continuum emission, maser emission or strong CS have been detected at these locations supports the idea that these young protostars and proto-clusters are probably not massive. The morphology of this younger generation of protostars and proto-clusters is compatible with a process of dynamical instabilities of the ionization front (Garcia-Segura & Franco 1996). Because the condensations do not seem to share the expansion of the ionized gas, another plausible explanation would be the radiation driven implosion of pre-existing molecular condensation. The morphology of the region at the rim of B2 where several YSO candidates are found resembles the cases where the collect and collapse process has be reported to be at work (Zavagno et al. 2006, 2007). The velocity distributions of the ionized and molecular gas have been proven valuable when studying the association of condensations and YSOs with H II regions (Pomarès et al. 2009).

B1 shows a thick dust shell with a combination of Class I and older Class II candidates, both in clusters and in isolation, farther away from the ionization front. Zavagno et al. (2007) report a similar result in their study of the RCW 120 region, explaining it in terms of a leak of radiation into the PDR.

A question arises after discussion of the impact of the various clusters on their immediate surroundings: what is the interplay between the high-mass stellar populations in this region? are Cl3, and especially Cl2, produced by the expansion of the H II region powered by Dolidze 25?

The powering clusters Cl2 and Cl3 are dominated by Class II candidates. It is therefore puzzling to detect younger Class I candidates in the direction of the central cluster Dolidze 25, the presumed oldest cluster in this region. In the case that these YSO candidates were associated to the cluster, these results would challenge the triggered SF scenario initially suggested by the multiple bubble morphology of S284, in particular the close location of Cl2 to the B1 shell. The UV field produced by the several O-type stars of Dolidze 25 must contribute to the photoevaporation of circumstellar material in nearby stars. However, YSO candidates have also been detected close to the young massive cluster NGC 6611 in the Eagle nebula (Indebetouw et al. 2007). The authors conclude that circumstellar disks must be fairly robust to the cluster environment around NGC 6611. Another possible explanation would be that these Class I objects are located at the border of the bubble, either in the foreground or in the background. Further support for this hypothesis could come from the detection of several Class II candidates in Fig. 6. These Class II sources would trace the stellar population associated with a large emission filament that crosses B1 in the northeast direction in our IRAC images and appears in absorption in our Hα image. The proximity *in projection* of this filament suggests that this or other structures in the line of sight could overlap with the cluster Dolidze 25. If the Class I objects detected near Dolidze 25 were not members, the cluster would be dominated by a stellar population of naked photospheres. A future radial velocity study of the stars around Dolidze 25 would aid in answering this question.

4.3.1. Dynamical ages of the H II regions

The exceptional symmetry of S284 allows a rough calculation of the dynamical age of the H II region using a zero-order approximation (i.e. a simple pressure driven expansion), using the strong shock approximation and assuming a constant-density medium. We convert the spectral types of the most certain members from the literature (see Table 2) into the corresponding Lyman continuum photon rate. Dolidze 25 and its associated H II region are

Table 2. Membership and Spectral Types of Dolidze 25. Column (1) indicates the star number following the notation of Moffat & Vogt (1975). (m) members, (n) non-members.

ID	Classification						
(1)	(2)	(3)	(4)	(5)	(6)	(7)	(8)
1	(m)	B0IV	B5(m?)		B5		(n)
2	(n)		A5(–)		A5		(n)
3	(n)		A0(–)		A0		(n)
4	(n)		B2(–)		F5†		(n)
5	(n)		B5(–)		A0†		(n)
6	(n)		A5(–)		A5		(n)
7	(n)		A0(–)		A0†		(n)
8	(n)		A5(–)		A2†		(Cl 2 m)
9	(m)	O9	A0(m)		A0		(Cl 2 m)
10	(m)	F2Iab	F0(m)		F5†		(n)
11	(n)		K2		K2†		(n)
12	(m)	B0III	B2(m)		B2		(Dol 25 m?)
13	(m)		B8(m)		B8		(Dol 25 m?)
14	(n)		B8(–)		B8		(Dol 25 m)
15	(m)	B0III	B8(m)	(m)	B8	O6‡	(Dol 25 m)
16a	(x)						(Dol 25 m)
16b	(m)			(m)	B8		(Dol 25 m)
17	(m)	B1V	B8(m)	(m)	B8	O5.5–O6.5‡	(Dol 25 m)
18	(m)		F5(m)	(m)	F5		(Dol 25 m)
19	(m)		A5(m)		A5		(Dol 25 m)
20	(n)		F5(–)		F5		(Dol 25 m)
21	(n)		F5(–)		F5		(Dol 25 m)
22	(m)		A5(m)	(m)	A5	O8–O9‡	(Dol 25 m)
23	(n)						(n)
24			B8(m?)				(n)
25							(n)
26			K0(–)				(n)
27			F5(m)				(n)
28			F5(m)				(n)
31			F0(m)				(n)
32			F0(m)				(n)
33			B8(m)				(n)
34			F5(m)				(n)

(2) Moffat & Vogt (1975), (3) Moffat et al. (1979b), (4) Babu (1983), (5) Turbide & Moffat (1993), (6) WEBDA Open Cluster Database http://obswww.unige.ch/webda, (7) Lennon et al. (1990) (8) This work, † Spectral type classification from Cannon & Mayall (1949), ‡ Spectral type determination following Martins et al. (2005)

considered separately from Cl2 and its compact ionized region. Adopting an isothermal sound speed ~0.4 km s^{-1}, a recombination coefficient ~3 $\times 10^{-13}$ cm^3 s^{-1} and the estimated electronic density n$_e$ ~ 100 cm^{-3} (Shaver et al. 1983), we derive a dynamical age < 3.8 Myr for B1. In the case of the compact H ii region bound by B2, we assume n$_e$ ~ 2$\times 10^3$ cm^{-3} and a sound speed ~0.4 km s^{-1}, rendering a dynamical age < 1.8 Myr.

4.3.2. Comparison to isochrones and evolutionary tracks

We attempted a quantitative age analysis of the clusters Dolidze 25 and Cl2. For this purpose, we converted the photometry of the bright stellar population obtained with INT/WFC to the standard Johnson-Cousins photometric system (Deeg et al., private communication). We combined these data with the VIMOS photometry in the *R* and *I* bands of the faint population (Cusano et al. 2008). The CMDs of both regions are presented in Fig. 9. The population around Dolidze 25 exhibits a main sequence, and even a hint of lower-mass pre-main sequence in the CMD. This is not the case for Cl2, where no distinctive features are detected in the CMD probably due to the poor statistics. The field around Dolidze 25 is not fully covered to the north of the cluster by the VIMOS observations. This could explain the void of sources detected at I ~16 mag in the left panel of Fig. 9. The fit of a log(age[yr])= 6.75 isochrone to the blue part of the main sequence renders an E($R-I$)= 0.5 mag, considering a distance of 5 kpc.

The atmospheric parameter determination for source #22 (Lennon et al. 1990) secures an age upper limit for the cluster of 6.2±0.6 Myr (assuming a coeval stellar population). This estimate was obtained via comparison to a 15 M$_{\odot}$-evolutionary track with Z=0.004 from Lejeune & Schaerer (2001), although source #22 is located at the outskirts of Dolidze 25, while sources #15 and #17 belong to the high-stellar-density core of the cluster. Source #15 is spectrally classified as a middle O-type dwarf star, while star #17 appears as a more evolved hot star of spectral type III or Ib (Lennon et al. 1990). Their positions in the CMD reveal the presence of differential extinction toward the centre of Dolidze 25, detected also in the V vs. ($B-V$) diagram. Since the masses derived from atmospheric models are particularly uncertain for stars hotter than 35000 K, no comparison to an evolutionary track is attempted. Nevertheless, the presence of an O6V star (#15) confirms that Dolidze 25 is younger than 5 Myr.

The optimal isochrone fit to the stellar population of Cl2 in Fig. 9*(right panel)* indicates that it is also approximately 5 kpc away. We use the less certain spectral type classification of source #9 as O9V (Moffat et al. 1979b) and the comparison to a 15 M$_{\odot}$-evolutionary track to establish that the cluster must be younger than 1.0±1.0 Myr.

These results for Dolidze 25 and Cl2 are in good agreement with the dynamical ages estimated in the previous section from the correspondent H ii regions. Moreover, in the case of Cl2, the detection of several Class II objects within the cluster is compatible with the estimated age.

The age estimates for the clusters Dolidze 25 and Cl2 are consistent with the inferred dynamical ages of their respective H ii regions. This translates into an age spread of approximately 3 Myr between the two clusters. Considering the ~20 pc separation between them, S284 lies on the age spread–linear size relationship described by Elmegreen (2000) for the LMC clusters. This correlation is explained as the result of the rapid formation of self gravitating sub-clumps of a larger cloud complex. In this context, these results hint that the formation of the massive clusters in S284 is not necessarily triggered.

5. Conclusions

In this paper we have presented newly obtained IRAC/Spitzer and Hα/INT observations of S284. These observations show – at a very detailed level– a relatively undisturbed isolated site of high-mass star formation. We presented an overview of the young stellar content of this region and sketched a scenario for the evolution of this region, considering its morphology.

Our IRAC maps show the newly discovered dust diffuse component of the nebula, which allows the investigation of a multiple-bubble morphology. Since this sort of structure has recently been explained in terms of triggered star formation, we analyse the population and morphologycal features as proxies for their relative ages.

The dominant photospheric component traced by the filters IRAC 3.6 and IRAC 4.5 allows the detection of a cluster at the centre of the three H ii regions shown by our Hα map. These clusters must therefore harbour at least one high-mass star to blow such detectable ionized regions. Considering the remarkable symmetry of the bubbles and cluster centre positions, the morphologigal variations within the field are discussed in terms of the environmental conditions. Density variations along the field may play a major role in explaining the observed features.

Based on an IRAC colour-colour criterium on the photometry of point-like objects toward S284, we found a total of 155 Class I and 183 Class II candidates. Most of these young objects concentrate at the shells of the bubbles. The extrapolation of this analysis to the SEDs of integrated regions of extended emission yields the conclusion that six more embedded clusters are also located in the dust shell.

We have detected relative younger Class I candidates close to Dolidze 25 than the dominant Class II populations toward clusters Cl2 and Cl3. We considered a possible alignment of foreground or background, young YSOs in the line of sight of Dolidze 25, as well as a robust nature for low-mass disks, previously invoked for the case of NGC 6611 (Indebetouw et al. 2007). We studied the dynamical ages inferred from the H II regions. These are in good agreement with the ages inferred from the older stellar population of Dolidze 25 and Cl2 through comparison of optical photometry with isochrones and evolution tracks. Based on the age-spread and linear-separation argument, we discard the expansion of the B1 bubble as triggering the formation of Cl2 and most probably of Cl3.

Reddened younger luminous objects (Class I) are only detected at the vortices of cometary globules or elephant trunks, while a mixed population of Class I and Class II objects is present both in a clustered and a more scattered mode farther away from the ionization front inside B1. This suggested age gradient is even more pronounced considering the dominant Class II populations within Cl2 and Cl3 and the presence of Class I candidates at their respective shells. As a result, we see indications of triggered star formation between the powering clusters of the H II regions and the physical structures at their respective shells.

Processes such as radiation-driven implosion of pre-existing dense clumps, dynamical instabilities of the ionization front, and the collapse of the collected layer may explain the variety of morphologies observed in this region. We conclude that the S284 fulfils the necessary conditions for an in-depth study of triggered star-formation by expansion of its individual H II regions.

Acknowledgements. We thank M. Deleuil and the exoplanet team of CoRoT for providing their photometric data. We also thank the Spitzer helpdesk and F. Marleau for the discussions about IRAC photometry as well as J. Matute for endless discussions on the MOPEX pipeline. E. Puga kindly acknowledges the support of the GEPI, Observatoire de Paris during her stay. This publication makes use of data products from the Two Micron All Sky Survey, which is a joint project of the University of Massachusetts and the Infrared Processing and Analysis Center/California Institute of Technology, funded by the National Aeronautics and Space Administration and the National Science Foundation. This research has made use of the NASA/ IPAC Infrared Science Archive, which is operated by the Jet Propulsion Laboratory, California Institute of Technology, under contract with the National Aeronautics and Space Administration.

References

Allen, L. E., Calvet, N., D'Alessio, P., et al. 2004, ApJS, 154, 363
Babu, G. S. D. 1983, Journal of Astrophysics and Astronomy, 4, 235
Bachiller, R., Gomez-Gonzalez, J., Barcia, A., & Menten, K. M. 1990, A&A, 240, 116
Blitz, L., Fich, M., & Stark, A. A. 1982, ApJS, 49, 183
Boissier, S., Gil de Paz, A., Boselli, A., et al. 2007, ApJS, 173, 524
Brand, J., Cesaroni, R., Caselli, P., et al. 1994, A&AS, 103, 541
Cannon, A. J. & Mayall, M. W. 1949, Annals of Harvard College Observatory, 112, 1
Churchwell, E. 2002, ARA&A, 40, 27
Churchwell, E., Povich, M. S., Allen, D., et al. 2006, ApJ, 649, 759
Condon, J. J., Broderick, J. J., & Seielstad, G. A. 1991, AJ, 102, 2041
Cusano, F., Ripepi, V., Alcalá, J. M., et al. 2008, A&A
Deharveng, L., Zavagno, A., & Caplan, J. 2005, A&A, 433, 565
Deleuil, M., Meunier, J. C., Moutou, C., et al. 2009, AJ
Dolidze, M. V. 1961, Astronomicheskij Tsirkulyar, 223, 11
Ehlerová, S. & Palouš, J. 2005, A&A, 437, 101
Elmegreen, B. G. 1998, in Astronomical Society of the Pacific Conference Series, Vol. 148, Origins, ed. C. E. Woodward, J. M. Shull, & H. A. Thronson, Jr., 150
Elmegreen, B. G. 2000, ApJ, 530, 277
Fazio, G. G., Hora, J. L., Allen, L. E., et al. 2004, ApJS, 154, 10
Fich, M., Dahl, G. P., & Treffers, R. R. 1990, AJ, 99, 622
Garcia-Segura, G. & Franco, J. 1996, ApJ, 469, 171
Harju, J., Lehtinen, K., Booth, R. S., & Zinchenko, I. 1998, A&AS, 132, 211
Indebetouw, R., Robitaille, T. P., Whitney, B. A., et al. 2007, ApJ, 666, 321
Lejeune, T. & Schaerer, D. 2001, A&A, 366, 538
Lennon, D. J., Dufton, P. L., Fitzsimmons, A., Gehren, T., & Nissen, P. E. 1990, A&A, 240, 349
Lockman, F. J., Pisano, D. J., & Howard, G. J. 1996, ApJ, 472, 173
Makovoz, D. & Marleau, F. R. 2005, PASP, 117, 1113
Martayan, C., Floquet, M., Hubert, A. M., et al. 2008, A&A, 489, 459
Martín-Hernández, N. L., Peeters, E., Morisset, C., et al. 2002, A&A, 381, 606
Martins, F., Schaerer, D., & Hillier, D. J. 2005, A&A, 436, 1049
Meyer, M. R., Calvet, N., & Hillenbrand, L. A. 1997, AJ, 114, 288
Moffat, A. F. J., Jackson, P. D., & Fitzgerald, M. P. 1979a, A&AS, 38, 197
Moffat, A. F. J., Jackson, P. D., & Fitzgerald, M. P. 1979b, A&AS, 38, 197
Moffat, A. F. J. & Vogt, N. 1975, A&AS, 20, 85
Ojha, D. K., Tamura, M., Nakajima, Y., et al. 2004, ApJ, 616, 1042
Pandey, A. K., Sharma, S., & Ogura, K. 2006, MNRAS, 373, 255
Peeters, E., Hony, S., Van Kerckhoven, C., et al. 2002, A&A, 390, 1089
Plume, R., Jaffe, D. T., & Evans, II, N. J. 1992, ApJS, 78, 505
Pomarès, M., Zavagno, A., Deharveng, L., et al. 2009, A&A, 494, 987
Rieke, G. H. & Lebofsky, M. J. 1985, ApJ, 288, 618
Russeil, D., Adami, C., & Georgelin, Y. M. 2007, A&A, 470, 161
Sabbi, E., Smith, L. J., Carlson, L. R., et al. 2008, in IAU Symposium, Vol. 255, IAU Symposium, 157–161
Schlegel, D. J., Finkbeiner, D. P., & Davis, M. 1998, ApJ, 500, 525
Schmidt-Kaler, T. 1982, in Landolt-Börnstein, New Series (ed. K. Schaifers & H. H. Voigt (Springer-Verlag, Berlin), Vol. VI/2b, p. 451)
Shaver, P. A., McGee, R. X., Newton, L. M., Danks, A. C., & Pottasch, S. R. 1983, MNRAS, 204, 53
Shenoy, S. S., Carey, S. J., Noriega-Crespo, A., et al. 2007, in American Astronomical Society Meeting Abstracts, Vol. 210, American Astronomical Society Meeting Abstracts, 12.01
Sicilia-Aguilar, A., Hartmann, L., Calvet, N., et al. 2006, ApJ, 638, 897
Stanimirovic, S., Staveley-Smith, L., van der Hulst, J. M., et al. 2000, MNRAS, 315, 791
Tokunaga, A. T. 2000, in Allen's Astrophysical Quantities (ed. A. N. Cox (4th ed; New York: AIP), 143)
Turbide, L. & Moffat, A. F. J. 1993, AJ, 105, 1831
Weaver, R., McCray, R., Castor, J., Shapiro, P., & Moore, R. 1977, ApJ, 218, 377
Wegner, W. 1994, MNRAS, 270, 229
White, R. J., Greene, T. P., Doppmann, G. W., Covey, K. R., & Hillenbrand, L. A. 2007, in Protostars and Planets V, ed. B. Reipurth, D. Jewitt, & K. Keil, 117–132
Whitney, B. A., Indebetouw, R., Bjorkman, J. E., & Wood, K. 2004, ApJ, 617, 1177
Wouterloot, J. G. A. & Brand, J. 1989, A&AS, 80, 149
Wouterloot, J. G. A., Henkel, C., & Brand, J. 1988, A&A, 191, 323
Zavagno, A., Deharveng, L., Comerón, F., et al. 2006, A&A, 446, 171
Zavagno, A., Pomarès, M., Deharveng, L., et al. 2007, A&A, 472, 835
Zinchenko, I., Pirogov, L., & Toriseva, M. 1998, A&AS, 133, 337